Anisotropy in the annihilation dynamics of umbilic defects in nematic liquid crystals

I. Dierking,[1,*] M. Ravnik,[2] E. Lark,[1] J. Healey,[1] G. P. Alexander,[2] and J. M. Yeomans[2]

[1]*University of Manchester, School of Physics and Astronomy, Schuster Building, Oxford Road, Manchester M13 9PL, United Kingdom*

[2]*Rudolf Peierls Centre for Theoretical Physics, University of Oxford, 1 Keble Road, Oxford, OX1 3NP, United Kingdom*

(Received 24 May 2011; revised manuscript received 25 December 2011; published 16 February 2012)

Umbilic defects of strength $s = \pm 1$ were induced in a nematic liquid crystal with negative dielectric anisotropy, confined to Hele-Shaw cells with homeotropic boundary conditions, and their annihilation dynamics followed experimentally. The speeds of individual defects of annihilating defect pairs with strengths of equal magnitude and opposite sign were determined as a function of several externally applied parameters, such as cell gap, electric field amplitude, frequency, and temperature. It was shown that annihilating defects do not approach each other at equal speeds, but that a speed anisotropy is observed, with the positive defect moving faster than the negative one. The defects move more slowly as the strength of the applied electric field or the cell gap is increased. The speed anisotropy is found to be essentially constant for varying external conditions which do not change the material properties of the liquid crystal material, i.e., confinement, electric field amplitude, or frequency. Only for applied conditions that change material properties, such as temperature changing viscosity, does the speed anisotropy vary. The annihilation dynamics was also simulated numerically giving good qualitative agreement with the experiments. Using insight gained from the simulations we interpret the defects' speed in terms of their overlap and the speed asymmetry as arising from backflow effects and anisotropy in the elastic constants.

DOI: 10.1103/PhysRevE.85.021703 PACS number(s): 61.30.Jf, 61.72.Cc

I. INTRODUCTION

The study of coarsening behavior has been a topic of considerable interest in condensed matter physics over many decades, both theoretically [1] and experimentally [2]. Material properties are often largely dependent on their formation history and thus on the coarsening of domain structures and the annihilation of defects. This behavior may be observed in a wide range of condensed matter systems, such as alloys, semiconductors, polymers, liquid crystals, complex fluids, or biologically engineered systems. Liquid crystalline materials in particular provide an ideal system to observe the dynamic behavior during defect annihilation. This is due to the very small values of their elastic constants, which imply defect extensions over several tens of micrometers [3], compared to atomic distances in solid state materials. Also, due to the inherent optical birefringence of liquid crystals, the annihilation process can easily be followed *in situ* on practical time scales through polarizing optical microscopy.

Liquid crystals [4,5] are anisotropic fluids, individual phases of which are thermodynamically located between the solid crystal and the isotropic liquid. Various phases exhibit different degrees of order, with the nematic phase being structurally the most simple, i.e., the liquid crystal phase with the highest degree of symmetry. The nematic phase exhibits solely orientational order of the long axis of rodlike molecules, the direction of orientation being referred to as the director, while the molecular centers of mass are isotropically distributed. It is generally the first liquid crystal phase to be observed on cooling from the isotropic melt. A common polarizing microscope texture of the nematic phase is the Schlieren texture [6], which can exhibit four different director configurations in the vicinity of topological defects of strength, $s = \pm 1/2$ and $s = \pm 1$. These defects are connected via a network of two- and fourfold brushes observed in polarizing microscopy, as shown in Fig. 1. The sum over all defect strengths of a large sample tends towards zero, and due to a minimization of the elastic contribution to the free energy, defects of equal strength and opposite sign attract each other and eventually annihilate, ideally resulting in a uniform director configuration.

The coarsening dynamics of liquid crystal defects has been studied before by several authors: Scaling laws describing point defect or string densities and defect separations have been measured. Experimental studies were largely related to string defects [7–10] and defect loops [10,11], but the annihilation of point defects was also investigated [12–14]. Other experiments were concerned with smectic C liquid crystals [15] (which exhibit only $s = \pm 1$ defects), and with nematic polymer systems [16,17]. Theoretical work and computer simulations [18–22] largely support the experimental findings of a scaling relation for the defect density of $\rho(t) \approx t^{-1}$ and defect separation of $D(t) \approx (t_0 - t)^{1/2}$, as t tends to t_0, the time to annihilation.

The formation of defects in liquid crystals is generally promoted through either temperature [12,15–17] or pressure quenches [9–12] across the isotropic-to-liquid-crystal phase transition. A sudden change of an intensive variable of state is employed to induce a phase transition, which is accompanied by the formation of defects in the liquid crystalline state. This investigation uses a different mechanism to induce topological defects in the nematic phase. A homeotropically aligned nematic of negative dielectric anisotropy is subjected to an applied electric field. Above a certain threshold an electric field induced director reorientation into the planar state is observed, accompanied by the formation of umbilic defects [4,23–25]. Umbilic defects are regions where the in-plane component of the director rotates through $\pm 2\pi$ ($s = \pm 1$). These are not true defects, however, in the sense that the director field is not singular, but rather is a localized region of escape where the director reorients parallel to the electric

*ingo.dierking@manchester.ac.uk

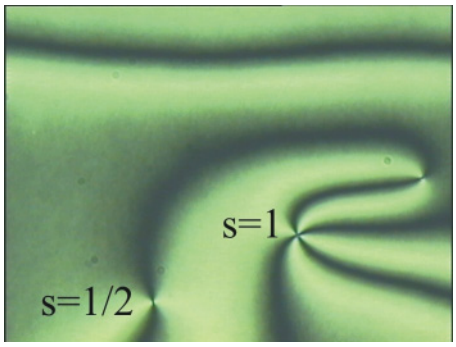

FIG. 1. (Color online) Nematic *Schlieren texture* illustrating connected defects of strength $s = \pm 1/2$ and $s = \pm 1$. On the large scale these form a network of connected defects with vanishing total charge and defects of equal magnitude and opposite sign annihilating to form a uniform director orientation. The image shown is approximately 350 × 500 micrometers.

field. This is analogous to the $s = \pm 1$ Schlieren defects except that the parallel alignment of the core matches smoothly onto the homeotropic surface anchoring instead of ending in singular points. Investigations of the annihilation dynamics of umbilical defects have the advantage that very well defined defect configurations can be studied, as only defects of strength $s = \pm 1$ are formed during electric field application. Nevertheless, studies of such systems are rare [13,14], with only one systematic investigation [26] reporting in detail on the dependencies of scaling exponents on external parameters.

It has been proposed on the basis of numerical simulations [27–29] that the annihilation of $s = \pm 1/2$ defects in nematic liquid crystals, and of $s = \pm 1$ defects in Sm*C* films [30], may be subject to an anisotropy in the speed at which defects of opposite strength approach each other. This speed anisotropy has recently been verified experimentally both for $s = \pm 1$ defects in a cholesteric with homeotropic anchoring [31] and for $s = \pm 1/2$ defects in a nematic under an applied electric field [32].

Here we extend these findings with an experimental investigation of defect annihilation for $s = \pm 1$ umbilical defects and verify an anisotropy in the defect speeds. The annihilation speeds of opposite strength defects, and their corresponding speed anisotropy while approaching each other, are detailed as a function of cell gap, applied electric field amplitude, frequency, and temperature. These experimental findings are complemented by numerical simulations. The dynamic effects of a variable strength of the electric field and variable cell thickness are qualitatively reproduced and explained. The defect dynamics is a consequence of a complex interplay between backflow coupling, the values of the elastic constants, director dynamics, and confinement.

II. EXPERIMENT

The liquid crystal employed in this investigation is a commercially available nematic mixture ZLI-2806 from Merck, Darmstadt, with negative dielectric anisotropy, $\Delta\varepsilon < 0$. Its phase sequence on cooling is given by Iso 100 N −20 Cryst., with temperatures given in °C. Sandwich cells with homeotropic alignment conditions (polyimide JALS 240-R40 from JSR Electronics, Leuven) and cell gaps between 6 and 50 μm were capillary filled at elevated temperatures in the isotropic phase. Defects were induced by electric square wave field application with a TTi TG1010 function generator, in combination with an in house built linear high voltage amplifier. Throughout observation of the defect annihilation process electric fields were kept applied. Electric field amplitudes were varied between 1 and 5 V μm^{-1} for frequencies in the range of 1–10^6 s^{-1}. At smaller field amplitudes the Freedricksz transition from homeotropic to planar is not completely achieved and defects are not formed. The temperature dependence of the annihilation dynamics, i.e., its qualitative variation with viscosity, was studied by regulating the temperature with a Linkham TMS91 hot stage and controller, providing relative temperature control to 0.1 °C at absolute temperature accuracies of ±1 °C. The defect annihilation process was followed by time resolved polarizing microscopy (Nikon Optiphot-pol) in conjunction with digital image acquisition. The digital camera employed (JVC KY-F1030) offered a time resolution of one image per second at a spatial resolution of 1280 × 960 pixels, corresponding to an actual image size of 520 × 390 μm^2. Subsequent digital image analysis was carried out with software IMAGETOOL3.0, developed at the University of Texas Health Science Center, San Antonio.

Two different methods for the analysis of defect annihilation speeds were employed. (i) Following the trajectories of a single defect pair at early times, i.e., far from the time of actual defect annihilation where the displacement can be approximated as being linear with time. We calculated the distance each defect traveled as a function of time, and subsequently determined the defect speeds from linear displacement versus time diagrams. As the time regime of approximate linear motion changes strongly with cell gap, care was taken that a linear time regime was analyzed. Although this is, in itself, a time consuming procedure, it does not take into account that neighboring defects, which are not involved in the individual annihilation process, may have an influence on the dynamics of the defect pair studied. (ii) The second procedure disregards the actual details of the motion of individual defect pairs, but averages over many annihilation incidents, considering initial and final spatial positions of many defect pairs over a given time interval. This method accounts for the influences of neighboring defects, but neglects the actual defect trajectories during the annihilation process, i.e., the fact that defect annihilation follows a square root law at times close to annihilation. In this analysis we avoided including any defect pairs which exhibited pinning effects at impurities. It is worth stressing that both analysis methods yield the same defect speed values within the limits of experimental error as stated in Sec. III. This is because the defects approach each other in an approximately linear fashion during the early times of the annihilation process and only exhibit square root behavior at times close to annihilation.

Errors from simply a linear fit to the selected early time experimental data regime would be underestimating the real errors on the experimental measurements. We thus estimated errors from the variation of results of five repeat experiments each for different initial conditions. This leads to a uniform error for all of the experimental data, which we

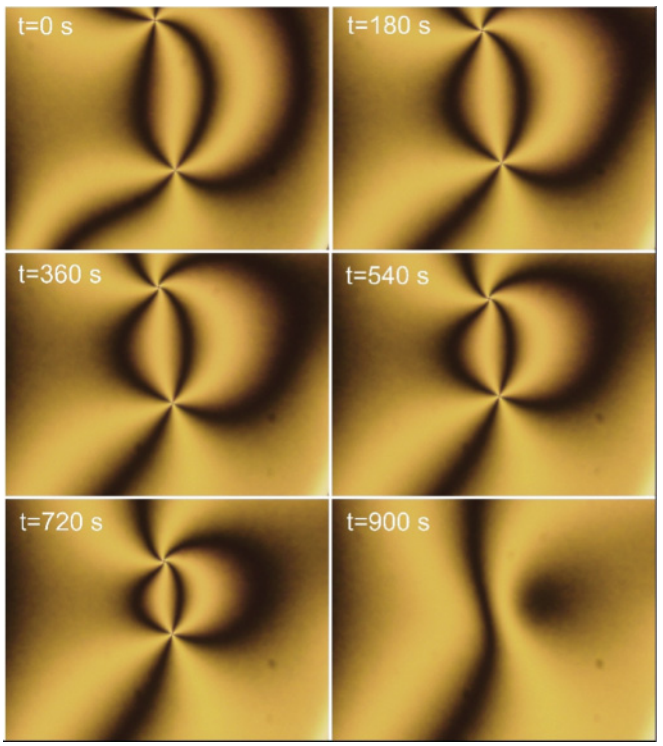

FIG. 2. (Color online) Exemplary texture series illustrating the time evolution of a pair of $s = \pm 1$ umbilical defects during the defect annihilation process. The applied field is 1 V μm $^{-1}$, frequency $f =$ 300 Hz, and cell gap $d = 50$ μm. Each image shown is approximately 350 $\times$ 500 micrometers.

believe provides a more realistic way to estimate experimental uncertainties.

III. RESULTS AND DISCUSSION

Figure 2 depicts an exemplary time series of an $s = \pm 1$ umbilical defect pair during the process of defect annihilation. The two topological defects are attracted to each other in order to annihilate and thus decrease the overall free energy of the sample by diminishing the elastic energy associated with the nonuniformities in the director field. The trajectory of the two defect cores is easily followed by polarized microscopy. A typical example is shown in Fig. 3. Already at this point it can clearly be observed that one defect is moving faster than its counterpart of opposite strength. Figure 4 depicts an example of the distance traveled by each of the $s = +1$ and $s = -1$ defects during the whole defect annihilation process. It can be seen that at early times, far from annihilation, the distance traveled is directly proportional to time, for both defects. This can also be verified by a log-log plot of the data at early times which gives a scaling exponent of 1.055 ± 0.005 for the fast $s = +1$ defect, and 1.007 ± 0.005 for the slower $s = -1$ defect. It is thus experimentally justified to estimate defect speeds at the early stages of annihilation via a linear distance-time relationship. At later times, closer to annihilation, the square root behavior seen in other defect annihilation experiments is recovered. The general behavior displayed in Fig. 4 is also observed for different cell gaps and varying applied conditions.

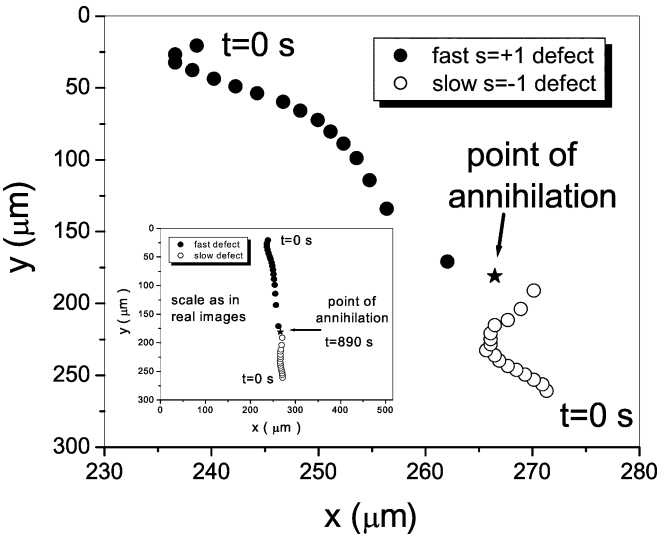

FIG. 3. Exemplary trajectories of a fast $s = +1$ (closed symbols) and a slow $s = -1$ (open symbols) defect during the annihilation process at a time resolution of 60 s. Already from this plot, it is clear that annihilating defects move at different speeds. The inset shows trajectories at the microscope image scale. The applied field is 1 V μm^{-1}, frequency $f = 300$ Hz, and cell gap $d = 50$ μm. (Note that this is an example at very low defect density and very slow defect annihilation, as observed for large cell gaps. For decreasing cell gap, the defect density increases, and the annihilation process becomes faster.)

The constant speed of the defects during annihilation, apart from at late times, differs from the behavior of free defects without a field [27,29]. However, it is consistent with the electric field experiments of Ref. [32] and is also qualitatively

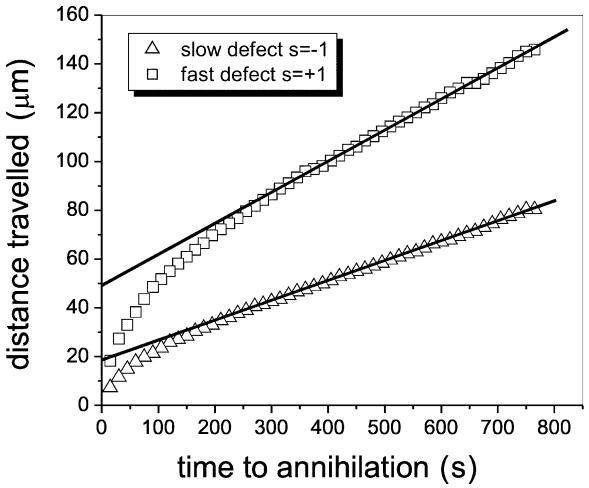

FIG. 4. During the early times of the defect annihilation process the distance that a defect travels is approximately linearly proportional to time, allowing an easy determination of the speeds of both approaching defects. The speeds of an annihilating defect pair are not equal in magnitude, but exhibit a certain defect speed anisotropy Δv. The applied field is 3 V μm^{-1}, frequency $f = 300$ Hz, and cell gap $d = 50$ μm. (Note that this is an example at very low defect density and very slow defect annihilation, as observed for large cell gaps. For decreasing cell gap the approximately linear speed regime extends much closer to the time of defect annihilation.)

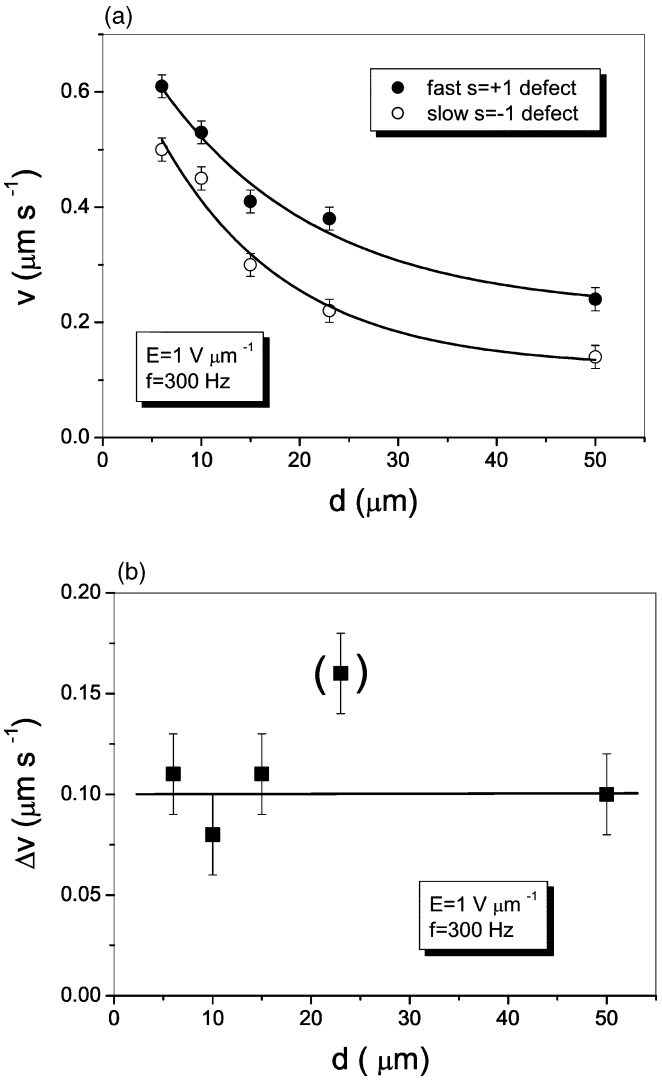

FIG. 5. (a) Defect speeds of the fast $s = +1$ (closed circles) and the slow $s = -1$ (open circles) defect during the annihilation process as a function of Hele-Shaw cell gap. (b) Corresponding defect annihilation speed anisotropy, which is practically independent of cell gap. (The case of the $d = 23$ μm data point is discussed in more detail in relation to Figs. 6 and 7.)

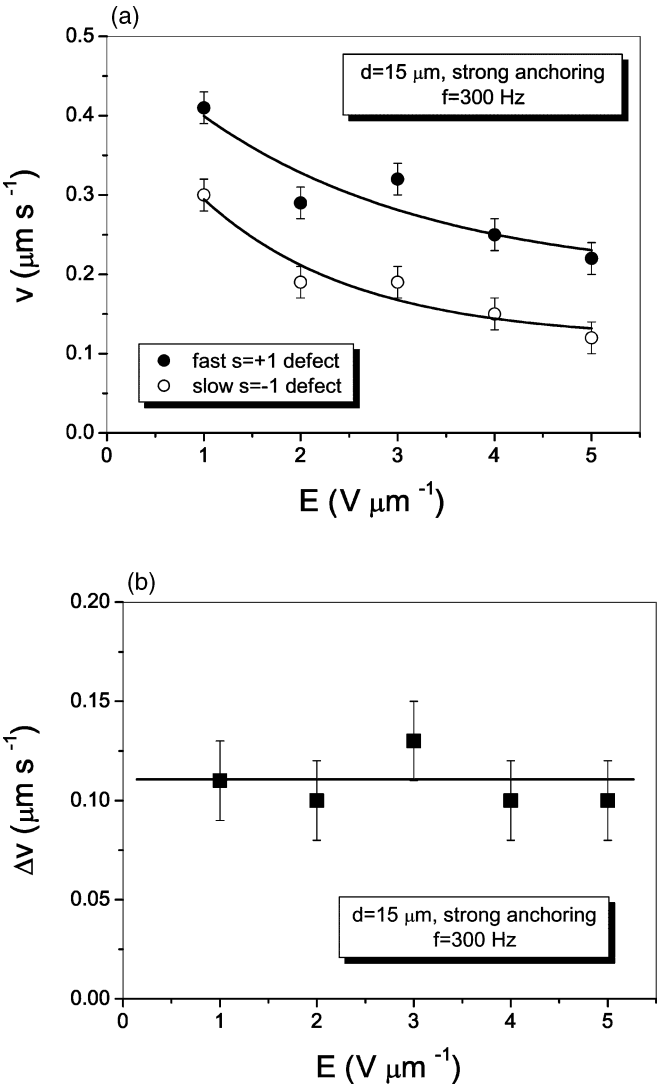

FIG. 6. (a) Defect speeds of the fast $s = +1$ (closed circles) and the slow $s = -1$ (open circles) defect during the annihilation process as a function of applied electric field amplitude for a cell with strong homeotropic anchoring conditions. (b) Corresponding defect annihilation speed anisotropy, which is practically constant for increasing field amplitude.

reproduced by our numerical simulations, as discussed in Sec. IV. We find that the crossover from linear to nonlinear behavior in the defect separation versus time sets in at defect separations L of approximately twice the cell gap d, i.e., at $L \approx 2d$, suggesting that the linear scaling behavior occurs when effects of the walls on the director distortion dominate over those due to the proximity of the defects.

The speeds are visibly different for the two annihilating defects. In the following, we will discuss the defect speeds during annihilation and the respective speed anisotropy in defect motion as a function of externally applied parameters, such as electric field, confinement, anchoring strength, and temperature. In Fig. 5 we show the dependence of the defect speeds on confining cell gap, which was varied over approximately one order of magnitude in size. The speed of both types of defects as they approach each other to annihilate decreases as the cell gap increases [Fig. 5(a)]. This suggests that defects in bulk samples annihilate more slowly, and may be understood on the basis that increased confinement increases the size of the region of distortion around the defects, leading to greater overlap between defects. The difference in defect speeds between the fast and the slow moving defects, Δv, on the other hand is independent of cell gap, as demonstrated in Fig. 5(b). This indicates that the effect of confining surfaces is the same for both defect types. (The case of the $d = 23$ μm cell with values in brackets will be discussed in more detail below. This represents a cell that was prepared differently from the others with respect to surface alignment treatment—the substrates were Octadecyltrimethoxysilane (OTMS) coated, possibly giving weaker anchoring, as also suggested by a lower threshold voltage).

Figure 6 depicts the speeds v and the anisotropy Δv of two annihilating defects as a function of applied electric field amplitude E for a cell with strong anchoring. The speed

for both types of defects decreases slightly with increasing electric field amplitude [Fig. 6(a)]. Nevertheless, the effect of the applied electric field amplitude is equivalent for both types of annihilating defects, which is exemplified by the fact that the speed anisotropy is independent of field amplitude [Fig. 6(b)]. We remark that the size of the region of director distortion around a defect depends strongly on the applied voltage, decreasing from tens of micrometers at very low voltages to tens of nanometers at high voltages. The larger extent of the deformation around the center of the defect for small voltages will cause a larger overlap between the defects and hence a faster annihilation.

These behavioral trends are sensitive to the anchoring conditions of the cell. The experimental data of Fig. 6 were taken using a cell with strong homeotropic anchoring conditions, and similar results were obtained for all the cells with strong anchoring. However, for the $d = 23$ μm cell, which was prepared with a different alignment agent and presumably weaker anchoring conditions, a quite different electric field amplitude dependence of the annihilation speeds as well as their anisotropy was seen. This is illustrated in Fig. 7. For relatively small applied electric field amplitudes $E < 3$ V μm^{-1}, the defect speeds of both defect types are practically constant, although different in magnitude. At larger electric field amplitudes of approximately $E > 3$ V μm^{-1} the defect speeds and the speed anisotropy show a strong increase. This may be due to the onset of electrohydrodynamic effects, which are suppressed by strong anchoring conditions. We should mention that we did not directly observe the development of electroconvective rolls, simply because we stopped measurements at the onset of seeing irregular motion within the liquid crystal at field and frequency parameters where electrohydrodynamics sets in. This parameter regime is outside of the current interest, experimentally, as well as from the perspective of computer modeling. The ionic charge relaxation covers a frequency regime to about 500 Hz, so that our measuring frequency of $f = 300$ Hz is right in the middle of that regime.

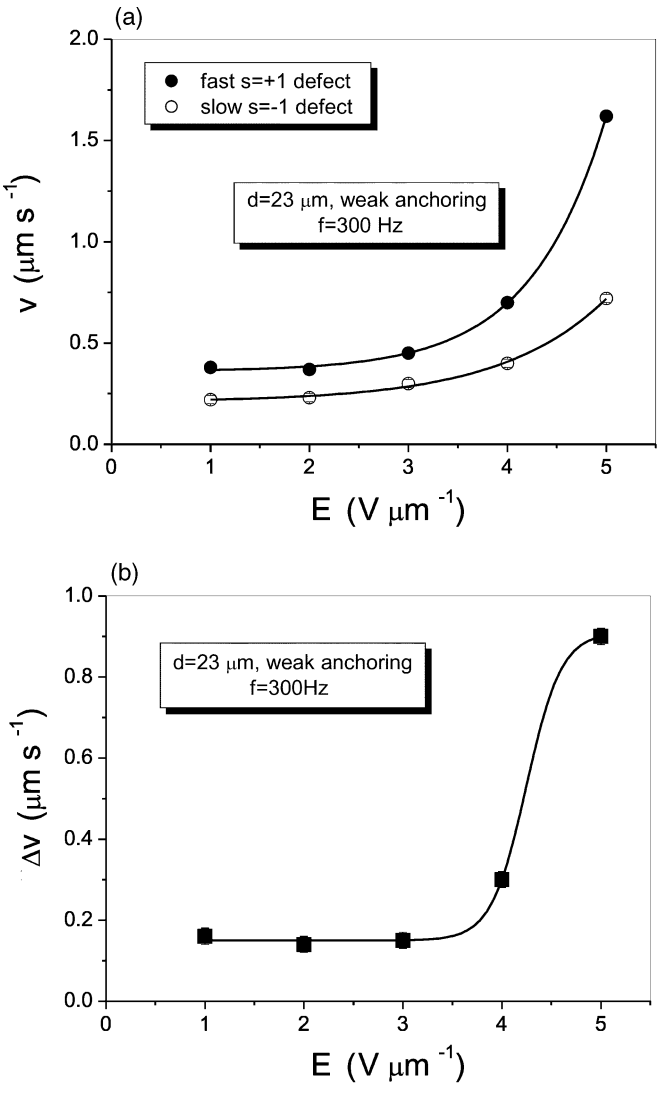

FIG. 7. (a) Defect speeds of the fast $s = +1$ (closed circles) and the slow $s = -1$ (open circles) defect during the annihilation process as a function of applied electric field amplitude for a cell with weak homeotropic anchoring conditions. (b) Corresponding defect annihilation speed anisotropy. At large applied electric fields $E >$ 3 V μm^{-1} the defect annihilation speed anisotropy Δv deviates from a constant value. This may be due to the onset of electrohydrodynamic effects, which are suppressed by strong anchoring conditions.

Another applied electric field parameter that was varied was the applied square wave frequency f, which was changed over more than five orders of magnitude, between 1 and 10^6 Hz (Fig. 8). Although the two approaching defects clearly show different speeds (open versus closed symbols), these speeds were constant and independent of the applied electric field frequency, as depicted in Fig. 8(a). Consequently, the speed anisotropy Δv was also independent of applied field frequency, as demonstrated in Fig. 8(b). This behavior can be understood by the dielectric nature of the electric field interaction with nematic liquid crystals. The interaction between the electric field and the liquid crystal is proportional to E^2, thus an applied ac square wave field acts effectively like a dc field (except when acting on ions). These results suggest that ionic contamination, which is always present in any liquid crystal, does not play any significant role in this experiment.

Finally, we investigated the defect annihilation behavior and its speed anisotropy as a function of temperature T. Temperature variation of the liquid crystal between 30 °C and 90 °C will primarily affect the viscosity of the material. Decreases of the orientational nematic order parameter on increasing temperature in the regime investigated will not influence the macroscopic behavior of defect coarsening significantly. This is because the largest changes of the order parameter are observed within the vicinity of a few degrees of the phase transition. Our experimental investigations are focused onto a temperature regime quite far below the clearing point at reduced temperatures of $(T_C – T) = 10$–70 K.

The speed at which annihilating defects approach each other increases exponentially with increasing temperature [Fig. 9(a)], primarily resulting from an Arrhenius-like decrease in material viscosity. Such behavior is observed for both types of defects, the fast $s = +1$ as well as the slow $s = -1$ one, as illustrated by the closed and open symbols in Fig. 9(a), respectively. As expected the defect speed anisotropy also increases exponentially, as illustrated in Fig. 9(b).

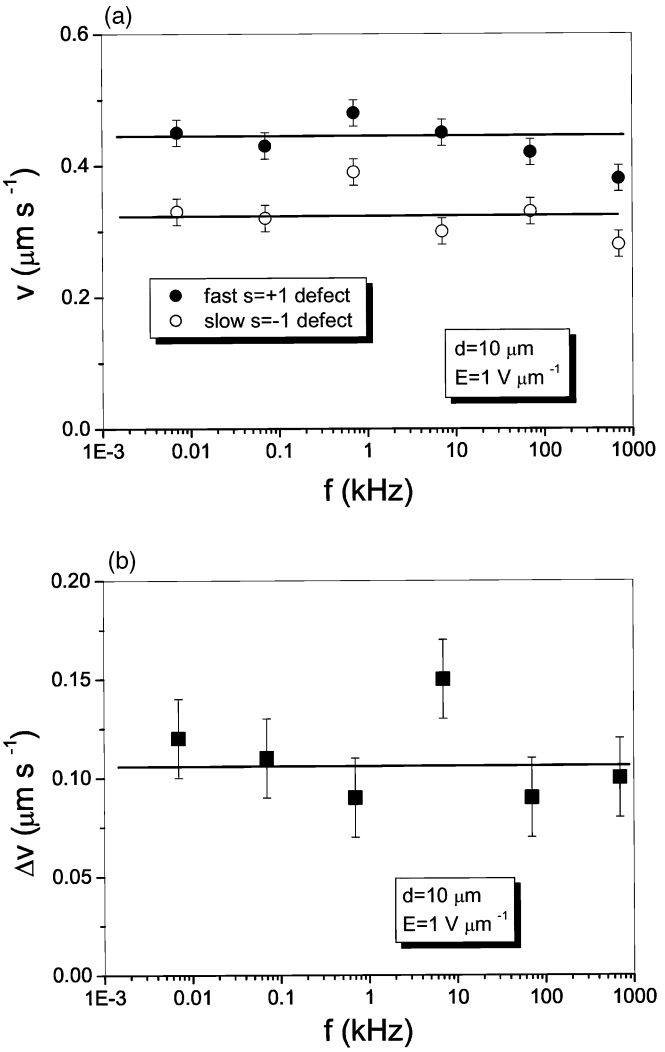

FIG. 8. Frequency dependence of (a) the defect speeds and (b) the corresponding defect speed anisotropy. Defect speeds are practically independent of the frequency of the applied electric field, due to the dielectric nature of the interaction between field and liquid crystal. The defect annihilation speed anisotropy is thus also independent of applied field frequency.

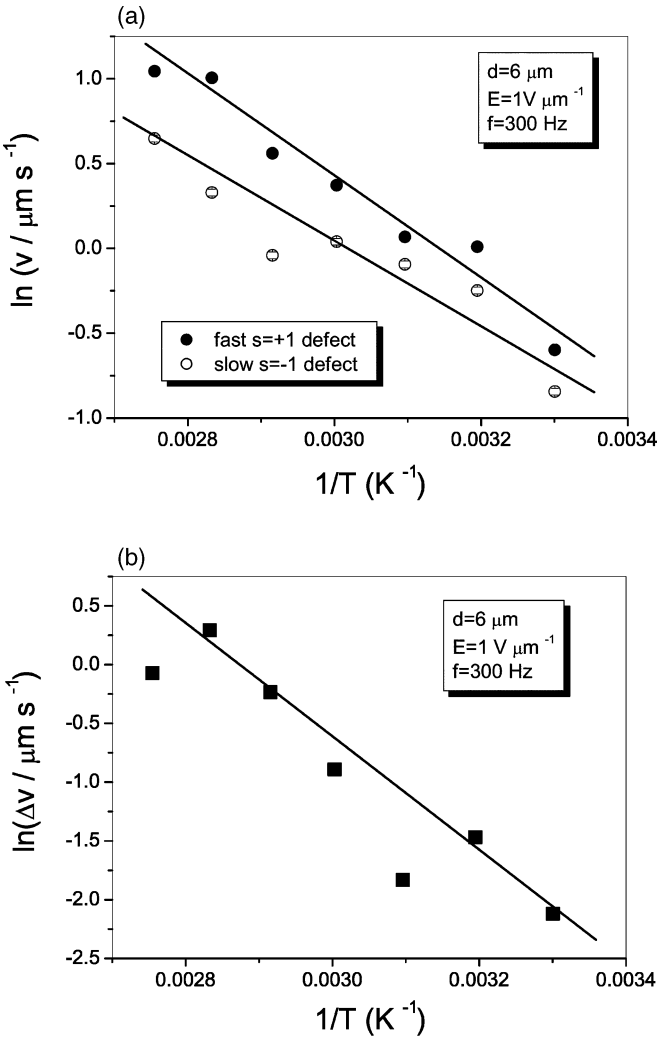

FIG. 9. Temperature dependence of (a) the defect speeds and (b) the annihilation defect speed anisotropy. Defect speeds increase exponentially with increasing temperature, due to an Arrhenius-like, exponential decrease of the liquid crystal viscosity. With temperature variation changing the material properties of the liquid crystal (primarily its viscosity) the defect annihilation speed anisotropy also changes with temperature.

An interesting observation from all of these systematic investigations is the fact that the speed difference between the fast and the slow moving defect is approximately constant at $\Delta v \approx 0.1\ \mu\text{m s}^{-1}$ for all externally applied parameter changes that do not directly influence the material properties of the liquid crystal, i.e., cell gap d [Fig. 5(b)], electric field amplitude E [Fig 6(b)], and frequency [Fig. 8(b)]. Only in the case where actual material properties are varied, such as viscosity, does the defect annihilation speed anisotropy Δv depend on external parameters, i.e., temperature [Fig. 9(b)]. In the case of weak anchoring [Fig. 7(b)], deviations may be attributed to possible electrohydrodynamic contributions at large applied electric field amplitudes ($E > 3\ \text{V}\ \mu\text{m}^{-1}$).

A point of discussion is that of the connection between the defect sign and the fast or slow moving defects. Numerical simulations of the annihilation of $s = \pm 1/2$ defects in nematics [27–29] and of $s = \pm 1$ defects in SmC films [30] and the simulations we report here all find the positive defect to move faster. Our experimental systems are obviously much less idealized than the numerical simulations, especially since we do not observe isolated defect pairs, but rather networks of many defects. Nevertheless, in numerous experiments, we also found that in the annihilation of umbilic defects the $s = +1$ defect is always faster than the $s = -1$ defect.

IV. SIMULATION

We now describe a numerical investigation of the dynamics of umbilic defect annihilation which complements these experimental results. Our simulations were performed using a hybrid lattice Boltzmann algorithm [33] to solve the Beris-Edwards [34] equations for the evolution of the liquid crystalline order parameter and fluid velocity. We focus our attention on an idealized situation in which a single pair of opposite strength defects attract each other and annihilate. The

calculations are performed in full three dimensions and mirror the experimental conditions qualitatively.

In our approach the order parameter for a nematic liquid crystal is taken to be a traceless symmetric second rank tensor $Q_{\alpha\beta}$ [4]. The director field n_α, which describes the principal alignment direction of the liquid crystal molecules, is given by the maximal eigenvector of $Q_{\alpha\beta}$. We describe the equilibrium properties of the liquid crystal with the Landau-de Gennes free energy density,

$$\mathrm{F} = \frac{L}{2}(\partial_\alpha Q_{\beta\gamma})^2 - \frac{\varepsilon_a \varepsilon_0}{3} E_\alpha Q_{\alpha\beta} E_\beta + \frac{A}{2} Q_{\alpha\beta}^2 + \frac{B}{3} Q_{\alpha\beta} Q_{\beta\gamma} Q_{\gamma\alpha} + \frac{C}{4}\left(Q_{\alpha\beta}^2\right)^2, \quad (1)$$

where L is a single elastic constant, ε_a is the microscopic dielectric anisotropy, ε_0 is the permittivity of free space, E_α is the applied electric field, and A, B, and C are liquid crystalline material constants. It is important to note that in systems of umbilic defects one needs to choose negative dielectric anisotropy $\varepsilon_a < 0$. The $\mathbf{Q}$-tensor evolves in time according to the equation

$$(\partial_t + \mathbf{u}\cdot\nabla)\,\mathbf{Q} - \mathbf{S}(\mathbf{W},\mathbf{Q}) = \Gamma \mathbf{H}, \quad (2)$$

where Γ is a collective rotational diffusion constant, $\mathbf{H}$ is the molecular field, and $\mathbf{S}$ represents a generalization of the convective derivative for rodlike molecules,

$$\mathbf{S}(\mathbf{W},\mathbf{Q}) = (\xi\mathbf{D} + \mathbf{\Omega})(\mathbf{Q} + \mathbf{I}/3) + (\mathbf{Q} + \mathbf{I}/3)(\xi\mathbf{D} - \mathbf{\Omega}) - 2\xi\,(\mathbf{Q} + \mathbf{I}/3)\,\mathrm{tr}(\mathbf{QW}). \quad (3)$$

In this expression $\mathbf{W}$ is the velocity gradient tensor, with components $W_{\alpha\beta} = \partial_\beta \mathrm{u}_\alpha$, $\mathbf{D}$ and $\mathbf{\Omega}$ are its symmetric and antisymmetric parts, respectively, and ξ is a constant related to the aspect ratio of the molecules that switches between the flow-aligning and flow-tumbling regimes.

We note that, as an alternative to the Q-tensor-based formalism used here, the annihilation dynamics of umbilic defects could also be modeled using a director-based Oseen-Frank formalism [4]. This is because the umbilic defects have no singular core, and therefore a vector order parameter—the director—can characterize the centers of the defects. The main advantage of the director-based approach is that it is less computationally demanding. However, the disadvantage is that it is unable to capture the changes in the nematic degree of order which emerge in the centers of the umbilic defects at stronger external fields and are relevant, for example, in particle and molecular manipulation [35].

The fluid velocity u_α satisfies the continuity and Navier-Stokes equations with a stress tensor generalized for liquid crystals,

$$\sigma_{\alpha\beta} = -p_0\delta_{\alpha\beta} + 2\eta D_{\alpha\beta} - \xi H_{\alpha\gamma}\left(Q_{\gamma\beta} + \frac{1}{3}\delta_{\gamma\beta}\right) - \xi\left(Q_{\alpha\gamma} + \frac{1}{3}\delta_{\alpha\gamma}\right) H_{\gamma\beta} + 2\xi\left(Q_{\alpha\beta} + \frac{1}{3}\delta_{\alpha\beta}\right) Q_{\gamma\delta} H_{\gamma\delta} + Q_{\alpha\gamma} H_{\gamma\beta} - H_{\alpha\gamma} Q_{\gamma\beta} - \partial_\alpha Q_{\gamma\delta} \frac{\delta \mathrm{F}}{\delta\,\partial_\beta Q_{\gamma\delta}}. \quad (4)$$

Here p_0 is the pressure and η is an isotropic viscosity. The presence of terms in the stress tensor involving the order parameter and the molecular field leads to backflow effects, whereby the relaxation of the order parameter induces a fluid flow, which subsequently affects the order parameter dynamics. In particular, these backflow effects contribute to the speed asymmetry in defect annihilation [27,29,31,32]. Within the simulations it is possible to turn off the backflow by decoupling the order parameter and fluid velocity fields. If this is done, $\mathbf{Q}$ evolves according to a purely relaxational Ginzburg-Landau equation, Eq. (2) with $\mathbf{u} = 0$.

The simulations are performed in a rectangular simulation box with cubic mesh, typically $200 \times 200 \times 100$ mesh points. Time-evolution equations for the order parameter tensor $Q_{\alpha\beta}$ are solved by an explicit finite difference scheme in time, whereas the generalized Navier-Stokes equation for the velocity field u_α is solved by a D3Q15 lattice Boltzmann method [33]. This lattice Boltzmann method discretizes the velocity field into 15 distinct symmetric velocity contributions (partial distribution functions) and propagates them in space according to collision rules, which give the Navier-Stokes-equation dynamics. Fixed homeotropic boundary conditions on the director field and no-slip boundary conditions for the velocity field are assumed at the top and bottom surface of the cell, and we use periodic boundary conditions in the lateral X,Y directions. Unless otherwise stated the following values for the material parameters are used. These are characteristic of a typical nematic liquid crystal rather than a quantitative match to the experiments [34,36,37]: $L = 4 \times 10^{-11}$N, $A = -0.172$ MJ/m^3, $B = -2.12$ MJ/m^3, $C = 1.73$ MJ/m^3, $\xi = 1$, $\varepsilon_a = -21$, $\Gamma = 7.29$/Pa s, the mesh resolution is $\Delta x = 10$ nm, time step $\Delta t = 0.24$ ms, and cell gap $d = 1$ μm. Here, note that that the typical cell gap in the simulations ($\sim$1 μm) is taken considerably smaller than the gap in experiments (6–50 μm), because of computational limitations. Therefore the comparison between experiments and simulations is qualitative.

A pair of opposite-sign umbilic defects has a distinct splayed field in the plane perpendicular to the cell walls (XZ) and dipolar director field in the lateral XY plane [see Fig. 10(a)]. Importantly, the director field is continuous everywhere and defects have no melted (isotropic) core; therefore, it is only the *projection* of the director field in the XY plane that has two discontinuous regions, i.e., the centers of the two umbilic defects. The order parameter tensor $Q_{\alpha\beta}$ of two neighboring umbilic defects can be initialized by an Ansatz for the director field:

$$\begin{aligned} n &= (\cos\phi\sin\Theta,\ \sin\phi\sin\Theta,\ \cos\Theta), \\ \phi(x,y) &= \arctan(y/x - x_{\mathrm{def}}) - \arctan(y/x + x_{\mathrm{def}}), \\ \Theta(z) &= c\pi\sin\left[\pi(z + d/2)/d\right]/2, \end{aligned} \quad (5)$$

which in Cartesian coordinates (x, y, z) creates a $+1$ radial hedgehog umbilic defect at (x_{def},0,0) and -1 hyperbolic umbilic defect at ($-x_{\mathrm{def}}$,0,0), within a cell of thickness d. The constant c,$-1 \leqslant c \leqslant 1$, determines the tilt in the central XZ plane of the cell and was taken to be $c = 0.6$.

Figures 10(b) and 10(c) show the positions X_p, X_m and velocities V_p, V_m of the two opposite-sign umbilic defects, presented in Fig. 10(a), as they annihilate in time. The dynamics of the two defects is nonuniform in time. They move at roughly constant speeds from the time of initialization ($t = 0$), but then accelerate in a short time interval just before

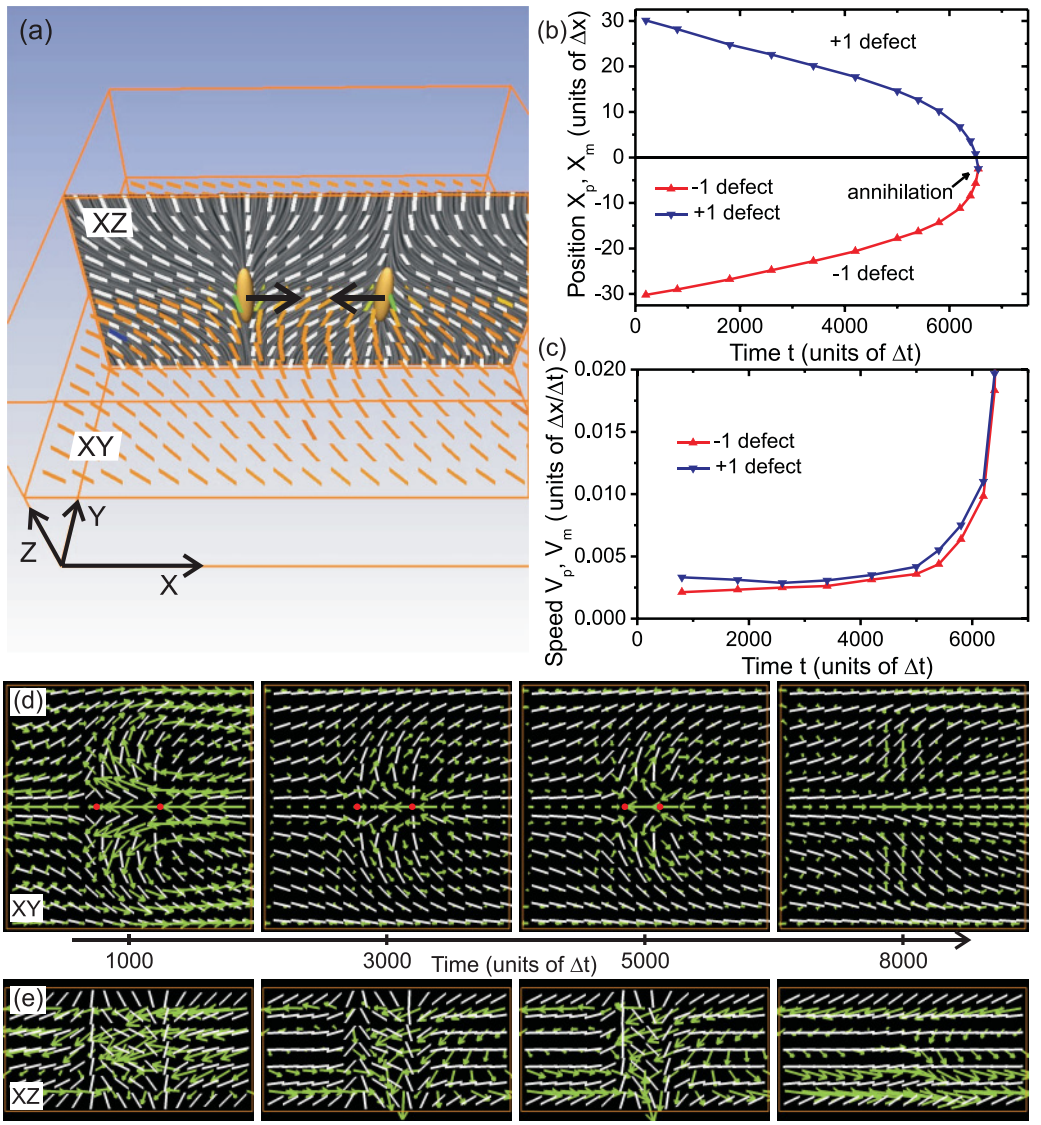

FIG. 10. (Color online) Simulated annihilation of $+/-1$ umbilic point defects. (a) Director field of two annihilating umbilic defects in the XY and XZ characteristic. The centers of the -1 defect (left) and $+1$ defect (right) are indicated in yellow. Note the coordinate axes. (b) Defect positions X_p and X_m of the $+1$ and -1 defects, respectively, as functions of time t. Defects annihilate at $t \sim 6500\Delta t$. (c) Defect speeds $V_p = \Delta X_p/\Delta t$ and $V_m = \Delta X_m/\Delta t$ of the $+1$ and -1 defects, respectively, as functions of time t. Note, the constant velocity for $t < 5000\Delta t$ and the asymmetry in the velocities of the $+1$ and -1 defect. (d),(e) Director profiles (in white) and velocity fields (green arrows) in the XY and XZ planes at various times during the annihilation dynamics. The left three panels show the snapshots before, and the right-most panels the snapshots after the annihilation. Red dots indicate the centers of the defects in the XY plane. Calculations were performed using a constant uniform electric field $E = 8\ \mathrm{V}/\mu\mathrm{m}$ along the z axis.

annihilation, in agreement with the experiments. The speeds of the two topologically distinct defects are found to be different. We can clearly attribute this to the backflow as performing calculations with only liquid crystalline dynamics (velocity field $u = 0$) gives no speed asymmetry in the one elastic constant approximation. As demonstrated in Figs. 10(d) and 10(e), the annihilating $+1$ defect (note the right red dot) is able to induce in its surrounding region a substantial material flow at all times, which is in contrast to the weak flow in the region of the -1 defect (note the left red dot). The stronger material flow of the $+1$ defect helps by advecting the local deformation field, making the $+1$ defect move faster. This again is in line with the experimental results (e.g., see Fig. 4).

The strength of the external electric field and the cell thickness are two elementary parameters that determine the dynamics of umbilic defects. We observe that when the electric field is increased both defects slow down [see Fig. 11(a)], again in good agreement with experiment [Fig. 6(a)]. Qualitatively, this behavior can be explained from the changes in the director profile of the two defects and their overlapping regions, which we present in Fig. 11(b). A larger electric field compresses the centers of the two defects making them more localized; note the increasingly narrower peaks in the director angle in Fig. 11(b) (bottom curves). The overlapping regions between the defects—the sources of the annihilation dynamics—are therefore shrunk and defects move more slowly. Interestingly,

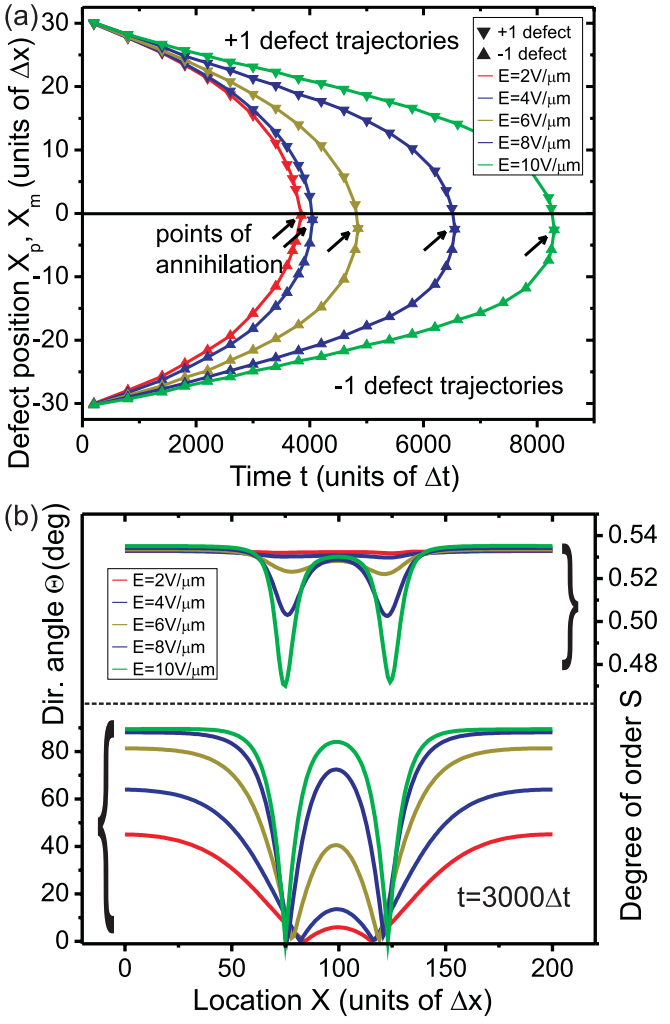

FIG. 11. (Color online) Annihilation dynamics of $+/-1$ umbilic defects for various strengths of the electric field E. (a) Defect positions X_p and X_m of the $+1$ and -1 defects, respectively, as functions of time t for various electric field strengths E. (b) Azimuthal angle Θ of the director [see also Eq. (5)] and nematic degree of order S along the X axis at time $t = 3000\Delta t$ for various electric field strengths. $\Theta = 0$ indicates the centers of the umbilic defects; $S = 0.533$ corresponds to the bulk nematic degree of order.

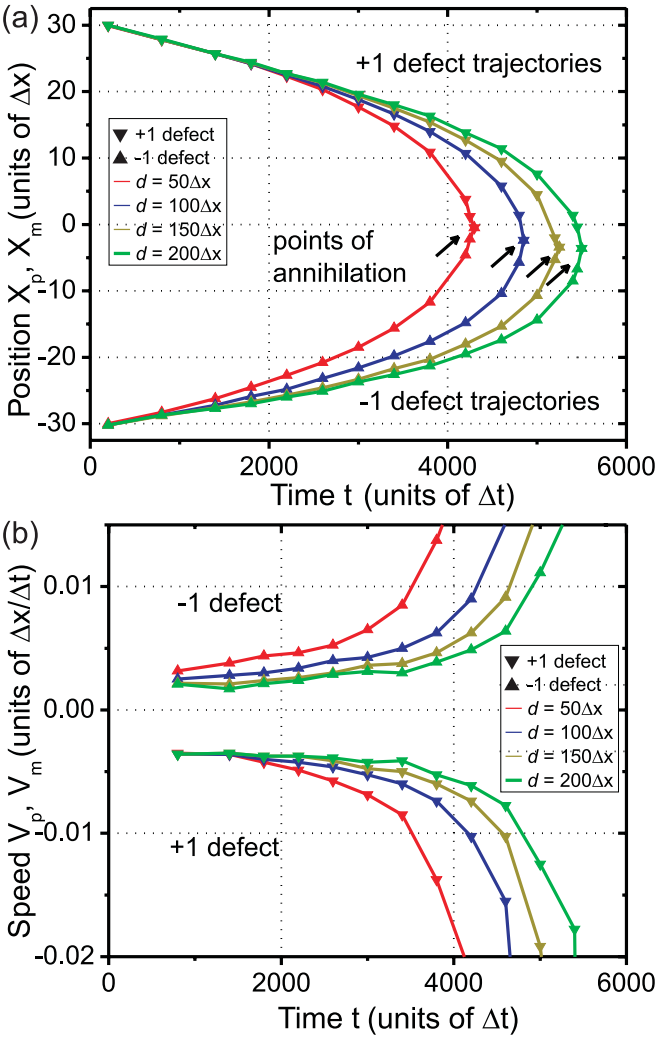

FIG. 12. (Color online) Annihilation dynamics of $+/-1$ umbilic defects for various cell thicknesses d. (a) Defect positions X_p and X_m and (b) defect speeds V_p and V_m of the $+1$ and -1 defects, respectively.

at larger electric fields, the degree of order in the centers of the two defects also starts to decrease [Fig. 11(b), top curves], which indicates the formation of weakly melted defect cores.

Figure 12 shows defect annihilation trajectories and defect speeds at constant electric field for different confinement, i.e., for various cell gaps d. We find that by increasing the cell gap (i) the defect speeds decrease and (ii) the asymmetry in the defect speeds increases. The decrease of the defect speeds can again be explained qualitatively by the changes in the director profile in the region between the two defects. By increasing the cell gap, the surface-imposed alignment of the director becomes weaker relative to the external electric field. (As an example of this, the Freedericksz threshold field E_{Freed} scales as $E_{\text{Freed}} \sim 1/d$.) Therefore, the electric field is able to localize the defect centers more, shrinking the director-overlap regions, which then leads to the slower dynamics of the defects. The increased asymmetry in the defect speeds, however, arises from the stronger backflow in wider cells. The maximum velocity of say, a pressure-driven, Poiseuille flow in the center of a confined cell $u_{\max}$ scales as $u_{\max} \sim d^2$ and although the driving mechanism for the flow is different here, this generic scaling, which is a consequence of confinement, is still relevant. Therefore, in wider cells, the relaxational dynamics of the director of the annihilating defects can initiate material flows which are larger in magnitude, leading to a larger asymmetry in the defect speeds. Again, the results on the effect of variable confinement are in good qualitative agreement with experiments (see Fig. 5).

In addition to backflow, the annihilation dynamics of defects is also affected by the anisotropy of the liquid crystalline elastic constants (K_1 splay, K_2 twist, K_3 bend), which also cause asymmetry in the defect speeds [38,39]. To assess the role of the elastic anisotropy, we perform additional numerical calculations, including both the full backflow and different values for the elastic constants (for details see [32]). The total free energy F [Eq. (1)] is generalized to include three elastic tensorial contributions characterized by tensorial elastic

constants L_i ($i = 1, 2, 3$), which directly map to the standard Frank elastic constants K_i ($i = 1, 2, 3$). (In the one elastic constant approximation $K_1 = K_2 = K_3$ and $L_2 = L_3 = 0$.)

In the annihilation of the $+1$ and -1 umbilic defects, the splay and bend elastic deformations are relevant. Therefore, by changing the ratio K_3/K_1 we can favor either bend ($K_3 < K_1$) or splay ($K_3 > K_1$) elastic deformation and test the role of the elastic anisotropy. We find that, for favored bend deformation, the elastic anisotropy drives the $s = -1$ defect faster than the $s = +1$ defect; by contrast, the backflow drives the $s = +1$ defects faster than the $s = -1$ ones. The effects of elastic anisotropy and the backflow effectively oppose one another, and for $K_1 = K_2 = K_3/2$ (at $E = 8$ V/μm) we observe very little speed anisotropy in the annihilation dynamics of the $s = +1$ and $s = -1$ umbilic defect.

For favored splay, however, as in our experiments, both the elastic anisotropy and the backflow drive the $s = +1$ defect faster than the $s = -1$ defect and they effectively add. For $K_1/2 = K_2 = K_3$ (at $E = 8$ V/μm), the anisotropy in elastic constants and the backflow each contribute $\sim$50% to the total speed anisotropy in the defect annihilation dynamics. Finally, to generalize, typical nematic materials have $K_3 > K_1$, therefore any observed anisotropy in the annihilation dynamics of defects stems from the backflow magnified by the elastic anisotropy.

V. CONCLUSIONS

The annihilation dynamics of pairs of $s = \pm 1$ umbilic defects were investigated both experimentally and numerically. The defects were observed to exhibit a speed anisotropy, induced by backflow and differences in the elastic constants, in agreement with previous simulations and experiments on other types of defects in liquid crystals [27–32]. Both the experiments and simulations showed the $s = +1$ defect moving faster.

The experiments systematically investigated the effects of confining cell gap, electric field strength and frequency, anchoring conditions, and temperature. The defect speed was found to increase as both the cell gap and the electric field strength were decreased. This is consistent in the sense that both factors act to increase the size of the region of distortion around the defects. It is natural to assume that increasing the extent of the distortion will lead to an increase in speed since there will be a greater overlap between the two defects in the annihilating pair. While the absolute speed was sensitive to external parameters, the speed anisotropy was essentially constant and only showed variation when the temperature was varied altering the viscosity of the material.

The simulations qualitatively confirm these findings. The linear relationship between displacement and time found experimentally at the early times of the annihilation process is reproduced. This suggests that the defect pairs analyzed experimentally were rather isolated and largely free from the influences of other defect pairs. The general experimental trends of defect speed decreasing as the electric field strength or cell thickness are increased are also seen in the simulations which provides support for our interpretation in terms of the variable localization of the umbilic defects. Finally, simulations indicate that at larger external fields partial, localized melting can occur in the centers of the defects.

ACKNOWLEDGMENTS

G.P.A. would like to thank Colin Denniston for beneficial discussions about the numerical simulations. M.R. acknowledges support of the EU under the Marie Curie Programme ACTOIDS.

[1] A. J. Bray, Adv. Phys. **43**, 357 (1994).
[2] L. Ratke and P. W. Voorhees, *Growth and Coarsening* (Springer, Berlin, 2002).
[3] M. Kléman, *Points, Lines and Walls* (Wiley, Chichester, 1983).
[4] P. G. de Gennes and J. Prost, *The Physics of Liquid Crystals*, 2nd ed. (Clarendon Press, Oxford, 1993).
[5] S. Chandrasekhar, *Liquid Crystals*, 2nd ed. (Cambridge University Press, Cambridge, 1992).
[6] I. Dierking, *Textures of Liquid Crystals* (Wiley-VCH, Weinheim, 2003).
[7] H. Orihara and Y. Ishibashi, J. Phys. Soc. Jpn. **55**, 2151 (1986).
[8] H. Orihara and T. Nagaya, J. Phys. Soc. Jpn. **56**, 3086 (1987).
[9] I. Chuang, R. Durrer, N. Turok, and B. Yurke, Science **251**, 1336 (1991).
[10] I. Chuang, N. Turok, and B. Yurke, Phys. Rev. Lett. **66**, 2472 (1991).
[11] I. Chuang, B. Yurke, A. N. Pargellis, and N. Turok, Phys. Rev. E **47**, 3343 (1993).
[12] A. N. Pargellis, N. Turok, and B. Yurke, Phys. Rev. Lett. **67**, 1570 (1991).
[13] T. Nagaya, H. Hotta, H. Orihara, and Y. Ishibashi, J. Phys. Soc. Jpn. **60**, 1572 (1991).
[14] T. Nagaya, H. Hotta, H. Orihara, and Y. Ishibashi, J. Phys. Soc. Jpn. **61**, 3511 (1992).
[15] A. N. Pargellis, P. Finn, J. W. Goodby, P. Panizza, B. Yurke, and P. E. Cladis, Phys. Rev. A **46**, 7765 (1992).
[16] D.-K. Ding and E. L. Thomas, Mol. Cryst. Liq. Cryst. **241**, 103 (1994).
[17] W. Wang, T. Shiwaku, and T. Hashimoto, J. Chem. Phys. **108**, 1614 (1998).
[18] H. Toyoki, Phys. Rev. A **42**, 911 (1990).
[19] M. Mondello and N. Goldenfeld, Phys. Rev. A **42**, 5865 (1990).
[20] H. Toyoki, Phys. Rev. E **47**, 2558 (1993).
[21] W. G. Jang, V. V. Ginzburg, C. D. Muzny, and N. A. Clark, Phys. Rev. E **51**, 411 (1995).
[22] C. Liu and M. Muthukumar, J. Chem. Phys. **106**, 7822 (1997).
[23] A. Rapini, J. Phys. (Paris) **34**, 629 (1973).
[24] A. Saupe, Mol. Cryst. Liq. Cryst. **21**, 211 (1973).
[25] R. B. Meyer, Mol. Cryst. Liq. Cryst. **16**, 355 (1972).
[26] I. Dierking, O. Marshall, J. Wright, and N. Bulleid, Phys. Rev. E **71**, 061709 (2005).
[27] G. Tóth, C. Denniston, and J. M. Yeomans, Phys. Rev. Lett. **88**, 105504 (2002).

[28] G. Tóth, C. Denniston, and J. M. Yeomans, Phys. Rev. E **67**, 051705 (2003).
[29] D. Svensek and S. Zumer, Phys. Rev. E **66**, 021712 (2002).
[30] D. Svensek and S. Zumer, Phys. Rev. Lett. **90**, 155501 (2003).
[31] P. Oswald and J. Ignés-Mullol, Phys. Rev. Lett. **95**, 027801 (2005).
[32] C. Blanc, D. Svensek, S. Zumer, and M. Nobili, Phys. Rev. Lett. **95**, 097802 (2005).
[33] C. Denniston, D. Marenduzzo, E. Orlandini, and J. M. Yeomans, Philos. Trans. R. Soc., A **362**, 1745 (2004).
[34] A. N. Beris and B. J. Edwards, *Thermodynamics of Flowing Systems* (Oxford University Press, Oxford, 1994).
[35] S. Samitsu, Y. Takanishi, and J. Yamamoto, Nat. Mater. **9**, 816 (2010).
[36] K. Skarp, S. T. Lagerwall, and B. Stebler, Mol. Cryst. Liq. Cryst. **60**, 215 (1979).
[37] M. L. Magnuson, B. M. Fung, and J. P. Bayle, Liq. Cryst. **19**, 823 (1995).
[38] E. I. Kats, V. V. Lebedeva, and S. V. Malinin, J. Exp. Theor. Phys. **95**, 714 (2002).
[39] J. Brugues, J. Ignes-Mullol, J. Casademunt, and F. Sagues, Phys. Rev. Lett. **100**, 037801 (2008).